

Identifying convex obstacles from backscattering far field data

Jialei Li^{*}

Xiaodong Liu[†]

Qingxiang Shi[‡]

Abstract

The recovery of anomalies from backscattering far field data is a long-standing open problem in inverse scattering theory. We make a first step in this direction by establishing the unique identifiability of convex impenetrable obstacles from backscattering far field measurements. Specifically, we prove that both the boundary and the boundary conditions of the convex obstacle are uniquely determined by the far field pattern measured in backscattering directions for all frequencies. The key tool is Majda's asymptotic estimate of the far field patterns in the high-frequency regime. Furthermore, we introduce a fast and stable numerical algorithm for reconstructing the boundary and computing the boundary condition. A key feature of the algorithm is that the boundary condition can be computed even if the boundary is not known, and vice versa. Numerical experiments demonstrate the validity and robustness of the proposed algorithm.

Keywords: inverse scattering; multi-frequency; sparse; backscattering; direct sampling method.

AMS subject classifications: 35P25, 45Q05, 78A46, 74B05

1 Introduction

Inverse obstacle scattering problems (ISPs) concern reconstructing unknown obstacles from measurements of scattered fields resulting from incident waves. These problems are of paramount importance in numerous applications, including radar, non-destructive testing, medical imaging, geophysical prospecting, and remote sensing. Substantial theoretical and computational advances have been made in the past decades for solving time harmonic ISPs, as comprehensively documented in the seminal monograph by Colton and Kress [12].

However, ISPs can not be considered completely solved, especially from a numerical point of view, and remain the subject matter of much ongoing research. The fundamental difficulties in solving ISPs originate from their nonlinearity and ill-posed nature, which yield significant challenges for numerical computations. In recent decades, non-iterative reconstruction methods

^{*}School of Mathematical Sciences, University of Chinese Academy of Sciences, Beijing 100049, China, and Academy of Mathematics and Systems Science, Chinese Academy of Sciences, Beijing 100190, China. Email: lijialei21@mails.ucas.ac.cn

[†]Academy of Mathematics and Systems Science, Chinese Academy of Sciences, Beijing 100190, China. Email: xdlou@amt.ac.cn

[‡]Corresponding author. Yau Mathematical Sciences Center, Tsinghua University, Beijing 100084, China. Email: sqxsqx142857@tsinghua.edu.cn

have drawn considerable research interest due to their computational efficiency and robustness, including the linear sampling method [11], the factorization method [24, 25], and more recently developed direct sampling methods [7, 20, 34, 35, 37, 45]. In particular, direct sampling methods inherit many advantages of the classical linear sampling method and factorization method, e.g., they are independent of any a priori information on the geometry and physical properties of the unknown objects. Moreover, the major advantage of direct sampling methods is their computational simplicity. Specifically, only the inner product of the measurement with some suitably chosen function is involved in the computation of the indicators of the direct sampling methods. This formulation renders the methods computationally efficient and remarkably stable against measurement noise.

A notable limitation of the aforementioned sampling methods discussed above is their qualitative nature. While they can effectively provide an approximation of the locations and shapes of the objects, they generally cannot determine the physical properties. This shortcoming significantly restricts their applicability in many practical scenarios, such as geophysical prospection, where precise determination of boundary conditions is often essential to identify the targets. In particular, the determination of the impedance parameter has been a central focus in ISPs research. To the best of our knowledge, it is always assumed that the boundary is known exactly to numerically solve the impedance parameter via either moment equation [8, 9, 10, 21, 22, 23] or probe-type methods [4, 5, 36]. The moment equation methods involve solving an integral equation of the first kind with noisy kernel and noisy right-hand sides. Therefore, such methods are highly unstable, particularly for variable impedance parameters. Probe-type methods offer a direct reconstruction formula for the impedance parameter at any boundary point but require measurements in all observation directions from all incident directions, which may be expansive in applications. For simultaneous reconstruction of both the boundary of the impedance parameter, we refer to gradient-based iterative methods, including the first regularized Newton method by Kress and Rundell [28] and more [18, 29, 31, 48].

The other limitation for direct sampling methods is that they are usually addressed for the full aperture scenario. However, practical implementations often must deal with the more challenging limited-aperture configuration and even backscattering data, i.e., one receiver and one transmitter with a fixed location are used to collect data. Currently, there is still a lack of global uniqueness results for inverse backscattering problems. For the case of Schrödinger operator and acoustic medium, it is shown that the local uniqueness is valid in a dense subset of compactly supported smooth potential (or medium) [15, 16, 53]. However, the global uniqueness remains open, although researchers are making progress on this subject [30, 44, 46, 47]. For inverse obstacle backscattering problems, there are even less results due to the high nonlinearity. Kress and Rundell [27] proved the local uniqueness near the unit disk by analyzing the Fréchet derivatives. Based on the high-frequency asymptotics of the far field, Shin [49] showed that the radius of a sound-soft ball can be uniquely determined via phaseless backscattering data and proposed a frozen Newton method for numerically reconstructing convex objects. The numerical methods using the multi-frequency backscattering far field patterns data back to Bojarski [3] via physical optics approximation. The well known Bojarski identity is proposed for reconstructing sound-soft or sound-hard obstacles. In a similar spirit, Arens, Ji, and Liu [1] developed a direct sampling method to reconstruct perfect conductors in the electromagnetic scattering context. Numerical experiments indicate that the high-frequency requirement could be relaxed to a certain extent but a rigorous proof is not known. There are also some numerical results using backscattering aperture data. We refer to [13] and [14] for the linear sampling method and the direct sampling

method, respectively, using limited-aperture single frequency "backscattering" data (in the sense that both the incident and observation directions are made on the same aperture). The size is well reconstructed, but the reconstruction is highly elongated down range. Li, Liu, and Wang [32, 33] developed a scheme for convex polygonal obstacles based on a certain local maximum behavior of high frequency far field pattern in the backscattering aperture.

This paper introduces a novel approach to ISPs through the analysis of point-wise backscattering data. We show that both the boundary geometry and the physical property of a convex obstacle can be uniquely determined from the multi-frequency backscattering far field patterns. To the best of our knowledge, this is the first rigorous uniqueness result for identifying all the parameters of an obstacle from the backscattering far field patterns. Furthermore, we design an efficient and robust algorithm for identifying the obstacles, which is the first solution for the simultaneous determination of both shape and impedance parameters from the backscattering far field data. In particular, we develop direct sampling methods that are capable of reconstructing the obstacle's boundary independent of boundary conditions, and vice versa.

The remainder of this paper is structured as follows: Section 2 outlines the problem setup, while Section 3 presents the proof of uniqueness. Numerical algorithms based on this proof are introduced in Section 4, and numerical examples are provided in Section 5 to illustrate the effectiveness of the proposed methods.

2 Problem setting

We begin with the formulations of the acoustic scattering problem. Let $k = \omega/c > 0$ be the wave number of a time harmonic wave, where $\omega > 0$ and $c > 0$ denote the frequency and sound speed, respectively. In the whole paper, we consider multiple frequencies in a bounded band, i.e.,

$$k \in (k_-, k^+),$$

with two positive wave numbers k_- and k^+ . Furthermore, let the incident field u^{in} be a plane wave of the form

$$u^{in}(x) = u^{in}(x, \theta, k) = e^{ikx \cdot \theta}, \quad x \in \mathbb{R}^n, \quad (2.1)$$

where $\theta \in \mathbb{S}^{n-1} := \{x \in \mathbb{R}^n : |x| = 1\}$ ($n = 2, 3$) denotes the direction of the incident wave.

The scattering of plane waves by impenetrable obstacle D involves finding the total field $u = u^{in} + u^s$ such that

$$\Delta u + k^2 u = 0 \quad \text{in } \mathbb{R}^n \setminus \overline{D}, \quad (2.2)$$

$$\mathcal{B}(u) = 0 \quad \text{on } \partial D, \quad (2.3)$$

$$\lim_{r:=|x| \rightarrow \infty} r^{\frac{n-1}{2}} \left(\frac{\partial u^s}{\partial r} - iku^s \right) = 0, \quad (2.4)$$

where \mathcal{B} denotes one of the following three boundary conditions

$$(1) \mathcal{B}(u) := u \quad \text{on } \partial D; \quad (2) \mathcal{B}(u) := \frac{\partial u}{\partial \nu} \quad \text{on } \partial D; \quad (3) \mathcal{B}(u) := \frac{\partial u}{\partial \nu} + ik\lambda u \quad \text{on } \partial D$$

corresponding the cases in which the scatterer D is sound-soft, sound-hard, and of impedance type, respectively. Here, ν is the unit outward normal on ∂D and $\lambda \in L^\infty(\partial D)$, $\inf \lambda(x) > 0$, is a positive real-value function on ∂D .

The well-posedness of the direct scattering problems (2.2)–(2.4) have been established and can be found in [12, 42]. Every radiating solution of the Helmholtz equation has the asymptotic behavior at infinity

$$u^s(x, \theta, k) = \frac{e^{ikr}}{r^{\frac{n-1}{2}}} \left\{ u^\infty(\hat{x}, \theta, k) + \mathcal{O}\left(\frac{1}{r}\right) \right\} \quad \text{as } r := |x| \rightarrow \infty, \quad (2.5)$$

uniformly in all directions $\hat{x} := x/|x| \in \mathbb{S}^{n-1}$ where the function $u^\infty(\hat{x}, \theta, k)$ defined on the unit sphere \mathbb{S}^{n-1} is known as the far field pattern of u^s with $\hat{x} \in \mathbb{S}^{n-1}$ denoting the observation direction. For $l \in \mathbb{Z}_+ \cup \{+\infty\}$, define

$$\Theta_l := \{\theta_j | j = 1, 2, \dots, l\} \subset \mathbb{S}^{n-1}.$$

In this paper, we consider the following two types of generalized backscattering direction sets:

- $\mathcal{A}_1 := \{(\hat{x}, \theta) \in \mathbb{S}^{n-1} \times \mathbb{S}^{n-1} | \hat{x} = Q\theta, \forall \theta \in \Theta_l\}$. The first data set \mathcal{A}_1 corresponds to the general backscattering experiment. Here, Q is a fixed rotation in \mathbb{R}^n . In particular, the data set \mathcal{A}_1 reduces to the classical backscattering experiment if $Q = -I$, where I is the identity matrix. The two sensors play the role of the source and the receiver. The measurements are then taken by moving these two sensors around the objects simultaneously.
- $\mathcal{A}_2 := \mathcal{A}_1^{(1)} \cup \mathcal{A}_1^{(2)} \cup \mathcal{A}_1^{(3)}$. The second data set \mathcal{A} is a union of three generalized data sets $\mathcal{A}_1^{(j)}, j = 1, 2, 3$ with different rotations Q_j and the same directions set Θ_l .

The inverse backscattering problem consists of the determination of the boundary ∂D and boundary condition \mathcal{B} from the far field patterns $u^\infty(\hat{x}, \theta, k)$ for all $(\hat{x}, \theta) \in \mathcal{A}_j$ with $j = 1$ or 2 and all wave numbers $k \in (k_-, k^+)$.

3 Uniqueness

In this section, we use high-frequency expansion of the far field pattern to derive uniqueness results from multi-frequency data. First, we recall Majda's asymptotics (Theorem 3.1) and extend it to the case of an impedance obstacle in \mathbb{R}^2 . We then prove our main results based on the high-frequency asymptotics.

3.1 Asymptotics of far field patterns

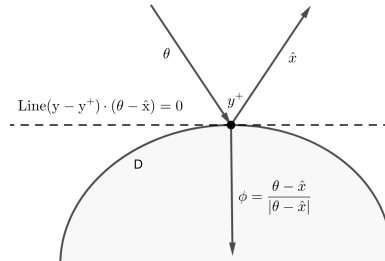


Figure 1: Physical optics diagram for incident direction θ and observation direction \hat{x} .

As shown in Figure 1, for any fixed $(\hat{x}, \theta) \in \mathcal{A}_j$, $j = 1, 2, 3$ satisfying $\hat{x} \neq \theta$, define the normal of the reflecting plane as

$$\phi(\hat{x}, \theta) := \frac{\theta - \hat{x}}{|\theta - \hat{x}|}. \quad (3.6)$$

For strictly convex obstacles, the Gauss map $G : \partial D \rightarrow S^{n-1}$ defined by $G(y) = \nu(y)$ is a bijective. In this case, we denote $\mathcal{G} : \mathbb{S}^{n-1} \times \mathbb{S}^{n-1} \rightarrow \partial D$ as

$$y^+(\hat{x}, \theta) = \mathcal{G}(\hat{x}, \theta) := G^{-1}(-\phi(\hat{x}, \theta)). \quad (3.7)$$

In other words, $y^+(\hat{x}, \theta)$ is the point at ∂D such that $\nu(y^+(\hat{x}, \theta)) = -\phi(\hat{x}, \theta)$. For clarity and brevity, we'll simply denote them as ϕ and y^+ when the context is unambiguous.

One main tool of the uniqueness proof is stated in the following theorem on the high-frequency asymptotic behavior of far field patterns.

Theorem 3.1. *Suppose that $D \subset \mathbb{R}^n$, $n = 2, 3$ is a smooth, strictly convex obstacle. Assume that any one of Dirichlet, Neumann, or impedance boundary conditions is satisfied on ∂D . Then, for any $\hat{x} \neq \theta$,*

$$\left| u^\infty(\hat{x}, \theta, k) - e^{iky^+ \cdot (\hat{x} - \theta)} \kappa^{-1/2}(y^+) R^\lambda(\hat{x}, \theta) \right| = O\left(\frac{1}{k}\right), \quad (3.8)$$

as $k \rightarrow \infty$. Here, $\kappa(y^+) > 0$ is the Gauss curvature at y^+ and

$$R^\lambda(\hat{x}, \theta) = -|\hat{x} - \theta|^{-\frac{n-1}{2}} \phi \cdot \hat{x} \frac{\lambda(y^+) + \phi \cdot \hat{x}}{\lambda(y^+) - \phi \cdot \hat{x}}$$

is the reflection coefficient concerned with the boundary condition. For the Dirichlet and Neumann boundary conditions, we set $\lambda = \infty$ and 0, respectively.

Theorem 3.1 was established by Majda [41] except for the impedance obstacles in two dimensions due to technical reasons. The results concerning such asymptotic expansion of the radiating solution of the Helmholtz equation can be traced back to Ludwig [40]. Majda [41] significantly extended these results through the construction of approximate solutions using the parametrix method developed by Taylor [52]. Majda specified the high-frequency asymptotics of the approximate solution, as well as the corresponding far field patterns, which is expected to dominate in (3.8).

When the discrepancy between the approximate and exact solutions becomes sufficiently small as $k \rightarrow \infty$ (see [41, Lemma 2.2]), one can rigorously deduce the asymptotic behavior of the true solution. Majda demonstrated this argument in the 3-dimensional scenario in his work. For Dirichlet and Neumann boundary conditions in 2 dimensions, he referred to earlier results from Morawetz [43]. The remaining challenge lies in establishing the estimates for the impedance boundary condition in two-dimensional settings, which we formally state as follows.

Lemma 3.2. *Consider the two-dimensional case, where u is a radiating solution in the exterior of obstacle D with a Lipschitz boundary, subject to the impedance boundary condition $\partial u / \partial \nu + ik\lambda u = g$. Then we have the following estimate:*

$$\|u\|_{L^2(B_R \setminus \overline{D})} \leq Ck^\alpha \|g\|_{L^2(\partial D)}.$$

Here, B_R is a disk of radius R centered at the origin such that $\overline{D} \subset B_R$, $\alpha > 0$, and C is a constant depending on R, α, λ .

Spence [50] proved this in 2014 when $\lambda > 0$ is a positive constant. Now we extend the work of Spence to the case of Lemma 3.2.

The fundamental solution to the Hemholtz equation in two dimensions is given by

$$\Phi_k(x, y) := \frac{i}{4} H_0^{(1)}(k|x - y|), x \neq y,$$

where $H_0^{(1)}$ denotes the Hankel function of the first kind of order zero. For any integrable function $\phi \in L^2(\partial D)$, we recall the acoustic single-layer potential S_k and acoustic double-layer potential D_k , defined respectively by

$$S_k \phi := \int_{\partial D} \Phi_k(x, y) \phi(y) ds(y), \quad x \in \mathbb{R}^2 \setminus \partial D,$$

and

$$D_k \phi := \int_{\partial D} \frac{\partial \Phi_k(x, y)}{\partial \nu(y)} \phi(y) ds(y) \quad x \in \mathbb{R}^2 \setminus \partial D.$$

We employ the notation $a \lesssim b$ if there is a constant C independent of k such that $a \leq Cb$. Now we state two key lemmas that will be essential for the proof of Lemma 3.2.

Lemma 3.3. *Let D be an obstacle with Lipschitz boundary. For any cutoff function $\chi \in C_c^\infty(\mathbb{R}^2)$, given $k_0 > 0$, we have*

$$\|\chi S_k\|_{L^2(\partial D) \rightarrow L^2(\mathbb{R}^2)} \lesssim k^{-\frac{1}{2}} \quad \text{and} \quad \|\chi D_k\|_{L^2(\partial D) \rightarrow L^2(\mathbb{R}^2)} \lesssim k^{\frac{1}{2}} \quad (3.9)$$

for all $k > k_0$.

We refer the reader to either [6, Theorem 2.15 and Theorem 2.16] or [50, lemma 4.3] for the proof. Note that the arguments in Lemma 3.3 is independent of the boundary conditions of the obstacle.

Lemma 3.4. *Let $u \in H_{loc}^1(\mathbb{R}^2 \setminus \overline{D})$ be a radiating solution to the Helmholtz equation $\Delta u + k^2 u = 0$ in $\mathbb{R}^2 \setminus \overline{D}$ satisfying the impedance boundary condition*

$$\frac{\partial u}{\partial \nu} + ik\lambda u = g$$

for some $\lambda \in L^\infty(\partial D)$, $\inf \lambda > 0$ and $g \in L^2(\partial D)$. Then the following estimates hold:

$$\left\| \frac{\partial u}{\partial \nu} \right\|_{L^2(\partial D)} \leq \left(1 + \frac{\sup \lambda}{\inf \lambda} \right) \|g\|_{L^2(\partial D)} \quad \text{and} \quad \|u\|_{L^2(\partial D)} \leq \frac{1}{k \inf \lambda} \|g\|_{L^2(\partial D)} \quad (3.10)$$

Proof. By Green's identity, we have

$$\begin{aligned} 0 &= \int_{B_R \setminus \overline{D}} \overline{u}(\Delta + k^2)u dy \\ &= k^2 \|u\|_{L^2(B_R \setminus \overline{D})}^2 + \|\nabla u\|_{L^2(B_R \setminus \overline{D})}^2 + \int_{\partial B_R} \frac{\partial \overline{u}}{\partial \nu} u ds(y) - \int_{\partial D} \frac{\partial \overline{u}}{\partial \nu} u ds(y). \end{aligned} \quad (3.11)$$

Taking the imaginary part of both sides and letting $R \rightarrow \infty$, it turns out that

$$\Im \int_{\partial D} \frac{\partial \bar{u}}{\partial \nu} u ds(y) = \lim_{R \rightarrow \infty} \Im \int_{\partial B_R} \frac{\partial \bar{u}}{\partial \nu} u ds(y) = k \|u^\infty\|_{L^2(S^1)}^2 > 0 \quad (3.12)$$

by the radiation condition (2.4). Substituting the impedance boundary condition into (3.12) gives

$$-k \int_{\partial D} \lambda(y) |u(y)|^2 ds(y) + \Im \int_{\partial D} \bar{g} u > 0. \quad (3.13)$$

Applying the Cauchy-Schwartz inequality yields

$$\|g\|_{L^2(\partial D)} \|u\|_{L^2(\partial D)} \geq k \inf \lambda \|u\|_{L^2(\partial D)}^2, \quad (3.14)$$

which establishes the second inequality in (3.10). The first inequality follows directly from the boundary condition and the triangle inequality. \square

We are ready to prove Lemma 3.2.

Proof of Lemma 3.2. By Green's formula [12, Theorem 2.5], the solution u can be expressed as

$$u = -S_k \frac{\partial u}{\partial \nu} + D_k u, \text{ in } \mathbb{R}^2 \setminus \bar{D}.$$

Applying the operator norm estimates from Lemma 3.3 and the Cauchy data estimates from Lemma 3.4, we obtain the following estimate

$$\begin{aligned} \|u\|_{L^2(B_R \setminus \bar{D})} &\leq \left\| S_k \frac{\partial u}{\partial \nu} \right\|_{L^2(B_R \setminus \bar{D})} + \|D_k u\|_{L^2(B_R \setminus \bar{D})} \\ &\lesssim k^{-\frac{1}{2}} \left\| \frac{\partial u}{\partial \nu} \right\|_{L^2(\partial D)} + k^{\frac{1}{2}} \|u\|_{L^2(\partial D)} \\ &\leq k^{-\frac{1}{2}} \left(1 + \frac{\sup \lambda + 1}{\inf \lambda} \right) \|g\|_{L^2(\partial D)}. \end{aligned}$$

This completes the proof of the lemma. \square

Theorem 3.1 holds universally for all boundary conditions in both two- and three-dimensional settings.

3.2 Uniqueness results

Based on Theorem 3.1, we establish the following uniqueness theorem using multi-frequency data in sparse directions.

Theorem 3.5. *Let $D \subset \mathbb{R}^n, n = 2, 3$ be a smooth, strictly convex obstacle with an arbitrary boundary condition given by (2.3). Consider an incident-observation direction pair (\hat{x}, θ) where $\hat{x} \neq \theta$, and assume the reflection coefficient $R^\lambda \neq 0$, i.e., $\lambda(y^+) \neq -\phi \cdot \hat{x}$. Then the following results hold:*

1. The line $y^+ \cdot (\hat{x} - \theta)$ and the combined parameter $\kappa^{-1/2}(y^+)R^\lambda(\hat{x}, \theta)$ are determined by the far field data $\{u^\infty(\hat{x}, \theta, k) | k \in (0, \infty)\}$.
2. Both the curvature $\kappa(y^+)$ and impedance parameter $\lambda(y^+)$ at the reflection point y^+ are determined by $\{u^\infty(\hat{x}_j, \theta_j, k) | k \in (0, \infty), j = 1, 2\}$ for $(\hat{x}_j, \theta_j), j = 1, 2$ such that $-\phi(\hat{x}_1, \theta_1) = -\phi(\hat{x}_2, \theta_2)$ is the normal vector at y^+ .

Proof. 1. Note that

$$\lim_{K \rightarrow \infty} \frac{1}{K} \int_K^{2K} u^\infty(\hat{x}, \theta, k) e^{-ikt} dk = \begin{cases} 0, & \text{if } t \neq y^+ \cdot (\hat{x} - \theta); \\ \kappa^{-1/2}(y^+) R^\lambda(\hat{x}, \theta), & \text{if } t = y^+ \cdot (\hat{x} - \theta). \end{cases} \quad (3.15)$$

Obviously, $y^+ \cdot (\hat{x} - \theta)$ and $\kappa^{-1/2}(y^+) R^\lambda(\hat{x}, \theta)$ are determined if $R^\lambda(\hat{x}, \theta) \neq 0$, which is satisfied by the assumption. Moreover, the support function of D at y^+ is determined because we know D in the half space $\{y \in \mathbb{R}^n | y \cdot (\hat{x} - \theta) < y^+ \cdot (\hat{x} - \theta)\}$.

2. It suffices to prove that $\lambda(y^+)$ is determined by

$$\kappa^{-1/2}(y^+) R^\lambda(\hat{x}_j, \theta_j), \quad j = 1, 2$$

First, $\lambda(y^+) \neq 0$ if $\kappa^{-1/2}(y^+) R^\lambda(\hat{x}_j, \theta_j) > 0$ and $\lambda(y^+) \neq \infty$ if $\kappa^{-1/2}(y^+) R^\lambda(\hat{x}_j, \theta_j) < 0$. By the assumptions on $\lambda(y^+)$, we can define the quotient

$$L := \frac{-|\hat{x}_2 - \theta_2|^{-\frac{n-1}{2}} \phi_2 \cdot \hat{x}_2 R^\lambda(\hat{x}_1, \theta_1)}{-|\hat{x}_1 - \theta_1|^{-\frac{n-1}{2}} \phi_1 \cdot \hat{x}_1 R^\lambda(\hat{x}_2, \theta_2)} = \frac{(\lambda(y^+) + \phi_1 \cdot \hat{x}_1)(\lambda(y^+) - \phi_2 \cdot \hat{x}_2)}{(\lambda(y^+) - \phi_1 \cdot \hat{x}_1)(\lambda(y^+) + \phi_2 \cdot \hat{x}_2)},$$

where $\phi_j = \phi(\hat{x}_j, \theta_j), j = 1, 2$. Obviously if $\lambda(y^+) = 0$ or ∞ then $L = 1$. Conversely if $L = 1$ and $\lambda \neq \infty$, then $\lambda = 0$. In consequence, we $\lambda(y^+)$ is determined if the boundary condition is Dirichlet or Neumann.

For the impedance case, $\lambda(y^+)$ is the solution of a quadratic equation

$$\lambda^2 + \frac{L+1}{L-1}(\phi_2 \cdot \hat{x}_2 - \phi_1 \cdot \hat{x}_1)\lambda - \phi_1 \cdot \hat{x}_1 \phi_2 \cdot \hat{x}_2 = 0.$$

The left-hand side takes the value $-\phi_1 \cdot \hat{x}_1 \phi_2 \cdot \hat{x}_2 < 0$ at $\lambda = 0$ and goes to $+\infty$ as $|\lambda| \rightarrow \infty$. Therefore, the equation has exactly one negative solution and one positive solution, i.e., $\lambda(y^+)$ is determined. □

Remark 3.6.

- Although the condition $\lambda(y^+) \neq -\phi \cdot \hat{x}$ is essential in Theorem 3.5, the arguments remain valid when additional data is available. Specifically, this condition fails for exactly one direction pair, and incorporating far-field patterns $u^\infty(\hat{x}^*, \theta^*, k)$ for an additional direction pair (\hat{x}^*, θ^*) with $-\phi(\hat{x}^*, \theta^*) = \nu(y^+)$ allows the method to proceed without this assumption. This suggests that the directions set \mathcal{A}_2 can stably identify the obstacle without a priori knowledge of λ .

- In the case where $\lambda(y^+) = -\phi \cdot \hat{x}$, equation (3.15) yields zero for all $t \in \mathbb{R}$, which is distinct from the case where $\lambda(y^+) \neq -\phi \cdot \hat{x}$. This allows us to still determine that $\kappa^{-1/2}(y^+)R^\lambda(\hat{x}, \theta) = 0$ in this scenario.
- For strictly convex obstacles ($\kappa > 0$), the boundary condition can be partially classified based on the sign of $\kappa^{-1/2}(y^+)R^\lambda(\hat{x}, \theta)$:
 - When $\kappa^{-1/2}(y^+)R^\lambda(\hat{x}, \theta) \geq 0$, the boundary must be either Dirichlet or impedance with $\lambda(y^+) \geq \phi \cdot \hat{x}$
 - When $\kappa^{-1/2}(y^+)R^\lambda(\hat{x}, \theta) \leq 0$, the boundary must be either Neumann or impedance with $\lambda(y^+) \leq \phi \cdot \hat{x}$

Thus, the sign of this quantity can eliminate either Dirichlet or Neumann boundary conditions for fixed directions \hat{x} and θ .

In conclusion, the line tangent to the obstacle at y^+ is determined except for the critical condition $\lambda(y^+) = -\phi \cdot \hat{x}$, in which the main term in the asymptotics (3.8) vanishes. Applying Theorem 3.5 to the data set \mathcal{A}_1 , we can derive the following uniqueness results.

Corollary 3.7. *Let D satisfy the assumptions in Theorem 3.5. Given far field data $\{u^\infty(\hat{x}, \theta, k) | (\hat{x}, \theta) \in \mathcal{A}_1, k \in (k_-, k^+)\}$, the following holds:*

1. The \mathcal{A}_1 -hull of D , defined as

$$D_{\mathcal{A}_1} := \bigcap_{(\hat{x}, \theta) \in \mathcal{A}_1} \{z \in \mathbb{R}^n | z \cdot \phi(\hat{x}, \theta) > y^+ \cdot \phi(\hat{x}, \theta)\}, \quad (3.16)$$

is uniquely determined.

2. For the case of infinitely many measurement directions ($l = \infty$), both the obstacle boundary ∂D and its boundary condition are uniquely determined.

Proof. 1. This is a direct consequence of Theorem 3.5.

2. Note that the generalized backscattering data $u^\infty(Qd, d, k)$ is analytic with respect to $d \in S^{n-1}$, which is proven in [17], which implies that our backscattering data is equivalent to full aperture backscattering data. Therefore, the convex hull of D , which is D itself, is determined. Once D is determined, the Gauss curvature $\kappa(x), x \in \partial D$ is also determined. Hence, $R^\lambda(x)$ is determined by Theorem 3.5, and $\lambda(x)$ follows. □

4 Numeric Algorithm

This section is devoted to introduce the reconstruction algorithm. For simplicity, we describe our algorithm for the two dimensional case. The three dimensional case can be obtained by proper modification. The far field patterns are obtained via the boundary integral equation method [12, 26]. We further perturb these synthetic data with relative random noise as follows:

$$u^{\infty, \delta}(\hat{x}, \theta, \omega) = u^\infty(\hat{x}, \theta, \omega) \left(1 + \delta [X_{\theta, \hat{x}, \omega} + iY_{\theta, \hat{x}, \omega}] \right), \quad (4.17)$$

where $X_{\theta, \hat{x}, \omega}, Y_{\theta, \hat{x}, \omega} \sim N(0, 1)$ are independent random variables, $N(0, 1)$ is normal distribution with mean zero and standard derivation one. If not stated otherwise, we take $\delta = 0.1$.

4.1 Determine the boundary condition

In this subsection, we introduce two methods to calculate the boundary conditions.

4.1.1 Determine the boundary condition without knowing ∂D

We begin with a method for computing the impedance coefficient λ without knowing the boundary ∂D . To do so, we use the multi-frequency far field patterns with direction set \mathcal{A}_2 . The theoretical basis is established in the following theorem.

Theorem 4.1. *For every $\hat{x}_0 \in \mathbb{S}^{n-1}$, we select three pairs (\hat{x}_j, θ_j) satisfying $-\phi(\hat{x}_j, \theta_j) = \hat{x}_0$, $j = 1, 2, 3$. Using $\left\{ |u^\infty(\hat{x}_j, \theta_j, k)| \mid k \in (k_-, k^+), j = 1, 2, 3 \right\}$, we can distinguish between the following two cases:*

- *The scatterer D is either sound-soft or sound-hard.*
- *The scatterer D is of impedance type, in which case $\lambda(\mathcal{G}(-\hat{x}_0, \hat{x}_0))$ can be additionally determined.*

Proof. According to (3.8), we define the following equations

$$\begin{aligned} L_j(\hat{x}_0) &:= \lim_{k_- \rightarrow \infty} \frac{|\hat{x}_1 - \theta_1|^{-\frac{n-1}{2}} \hat{x}_0 \cdot \hat{x}_1 \int_{k_-}^{k^+} |u^\infty(\hat{x}_j, \theta_j, k)| dk}{|\hat{x}_j - \theta_j|^{-\frac{n-1}{2}} \hat{x}_0 \cdot \hat{x}_j \int_{k_-}^{k^+} |u^\infty(\hat{x}_1, \theta_1, k)| dk} \\ &= \left| \frac{(\lambda - \hat{x}_0 \cdot \hat{x}_j)(\lambda + \hat{x}_0 \cdot \hat{x}_1)}{(\lambda + \hat{x}_0 \cdot \hat{x}_j)(\lambda - \hat{x}_0 \cdot \hat{x}_1)} \right| \quad j = 2, 3. \end{aligned} \quad (4.18)$$

Note that we regard λ as ∞ and 0 for the Dirichlet and Neumann boundary conditions. This implies that we know that $\mathcal{B}(u) = u$ or $\frac{\partial u}{\partial \nu}$ if $L_2(\hat{x}_0) = L_3(\hat{x}_0) = 1$, $\forall \hat{x}_0 \in \mathbb{S}^{n-1}$.

Otherwise, the scatterer D is of impedance type. Then, it is sufficient to consider the case that $\lambda(\mathcal{G}(-\hat{x}_0, \hat{x}_0)) - \hat{x}_0 \cdot \hat{x}_1 \neq 0$. Similar to the arguments in Theorem 3.5, for $j = 2, 3$ every equation (4.18) has two positive solutions, denoted by $\lambda(\mathcal{G}(-\hat{x}_0, \hat{x}_0))$ and λ_j^* , respectively. Without loss of generality, we assume that,

$$\frac{(\lambda(\mathcal{G}(-\hat{x}_0, \hat{x}_0)) - \hat{x}_0 \cdot \hat{x}_j)(\lambda(\mathcal{G}(-\hat{x}_0, \hat{x}_0)) + \hat{x}_0 \cdot \hat{x}_1)}{(\lambda(\mathcal{G}(-\hat{x}_0, \hat{x}_0)) + \hat{x}_0 \cdot \hat{x}_j)(\lambda(\mathcal{G}(-\hat{x}_0, \hat{x}_0)) - \hat{x}_0 \cdot \hat{x}_1)} = L_j(\hat{x}_0) \quad j = 2, 3.$$

Suppose that $\lambda_2^* = \lambda_3^* = \lambda^* > 0$ satisfies

$$\frac{(\lambda^* - \hat{x}_0 \cdot \hat{x}_j)(\lambda^* + \hat{x}_0 \cdot \hat{x}_1)}{(\lambda^* + \hat{x}_0 \cdot \hat{x}_j)(\lambda^* - \hat{x}_0 \cdot \hat{x}_1)} = -L_j(\hat{x}_0) \quad j = 2, 3.$$

Then, the equation

$$\frac{(\lambda - \hat{x}_0 \cdot \hat{x}_2)(\lambda + \hat{x}_0 \cdot \hat{x}_3)}{(\lambda + \hat{x}_0 \cdot \hat{x}_2)(\lambda - \hat{x}_0 \cdot \hat{x}_3)} = \frac{L_2(\hat{x}_0)}{L_3(\hat{x}_0)}.$$

has two positive solutions, which leads to a contradiction to the arguments in Theorem 3.5. Hence $\lambda_2^* \neq \lambda_3^*$. Then the impedance coefficient $\lambda(\mathcal{G}(-\hat{x}_0, \hat{x}_0))$ can be obtained because it appears twice among the four above solutions. \square

Numerically, we take $\alpha_1 = 8$ and $\alpha_2 = 10$, set

$$\delta k := \frac{k^+ - k_-}{M}, \quad \text{and} \quad k_m := k_- + m\delta k, \quad m = 0, 1, 2, \dots, M.$$

and compute

$$\mathcal{L}(\hat{x}, \alpha_j) := \frac{|\hat{x} - \theta|^{-\frac{1}{2}} \hat{x} \cdot \hat{x}}{|\hat{x}_j - \theta_j|^{-\frac{1}{2}} \hat{x} \cdot \hat{x}_j} \frac{\sum_{m=0}^M |u^{\infty, \delta}(\hat{x}_j, \theta_j, k_m)|}{\sum_{m=0}^M |u^{\infty, \delta}(\hat{x}, \theta, k_m)|}, \quad (4.19)$$

where $\hat{x} = -\theta$, $\hat{x}_j := Q_{\alpha_j} \theta_j$ and $\theta_j := R_{\alpha_j} \theta$ with

$$Q_{\alpha_j} := \begin{bmatrix} -\cos \frac{\alpha_j \pi}{16}, & \sin \frac{\alpha_j \pi}{16} \\ -\sin \frac{\alpha_j \pi}{16}, & -\cos \frac{\alpha_j \pi}{16} \end{bmatrix} \quad \text{and} \quad R_{\alpha_j} := \begin{bmatrix} \cos \frac{\alpha_j \pi}{32}, & \sin \frac{\alpha_j \pi}{32} \\ -\sin \frac{\alpha_j \pi}{32}, & \cos \frac{\alpha_j \pi}{32} \end{bmatrix}, \quad j = 1, 2. \quad (4.20)$$

First, we regard the boundary condition as a Dirichlet or Neumann boundary condition if

$$|\mathcal{L}(-\theta, \alpha_j) - 1| < \frac{\delta}{2} = 0.05, \quad \forall \theta \in \Theta_l, \quad j = 1 \text{ (or } 2). \quad (4.21)$$

Considering the 10% relative noise, we observe from Table 1 that the impedance coefficients $\lambda(\mathcal{G}(\theta, -\theta)) > 12.06$, $\forall \theta \in \Theta_l$ can be classified as Dirichlet boundary condition, while the impedance coefficients $\lambda(\mathcal{G}(\theta, -\theta)) < 0.06$, $\forall \theta \in \Theta_l$ can be classified as Neumann boundary condition. Therefore, the criteria (4.21) is reasonable to clarify whether the boundary condition is impedance type.

λ	0 (Neumann)	0.06	12.06	∞ (Dirichlet)
$u^\infty(d, d, 20)$	-3.3288 + 3.8856i	-3.5254 + 3.9288i	-4.3081 + 3.6514i	-4.3184 + 3.6405i
$u^\infty(d, -d, 20)$	-0.8189 + 0.2814i	-0.7255 + 0.2493i	0.7007 - 0.2172i	0.8278 - 0.2555i
$u^\infty(d, d, 50)$	-5.5900 + 6.0797i	-5.8112 + 6.1183i	-6.4356 + 5.8676i	-6.4422 + 5.8608i
$u^\infty(d, -d, 50)$	0.6111 + 0.6135i	0.5418 + 0.5442i	-0.5109 - 0.5262i	-0.6030 - 0.6217i

Table 1: The noise-free far field pattern at $d = (1, 0)^T$ for a disk $D = \{x \in \mathbb{R}^2, |x| \leq 1.5\}$ with different boundary conditions.

Second, for the impedance boundary condition, combining (4.18) and (4.19), we can obtain two positive solutions for each \hat{x}_1 and α_j by solving

$$\left| \frac{(\lambda - \hat{x} \cdot \hat{x}_j)(\lambda + 1)}{(\lambda + \hat{x} \cdot \hat{x}_j)(\lambda - 1)} \right| = \mathcal{L}(\hat{x}, \alpha_j). \quad (4.22)$$

Specifically, for $j = 1, 2$, we have

$$\lambda_{\alpha_j, \hat{x}}^{(1)} := \frac{1}{2} \left(\sqrt{\left[\frac{1 + \mathcal{L}(\hat{x}, \alpha_j)}{1 - \mathcal{L}(\hat{x}, \alpha_j)} (1 - \hat{x} \cdot \hat{x}_j) \right]^2 + 4\hat{x} \cdot \hat{x}_j} - \frac{1 + \mathcal{L}(\hat{x}, \alpha_j)}{1 - \mathcal{L}(\hat{x}, \alpha_j)} (1 - \hat{x} \cdot \hat{x}_j) \right),$$

$$\lambda_{\alpha_j, \hat{x}}^{(2)} := \frac{1}{2} \left(\sqrt{\left[\frac{1 - \mathcal{L}(\hat{x}, \alpha_j)}{1 + \mathcal{L}(\hat{x}, \alpha_j)} (1 - \hat{x} \cdot \hat{x}_j) \right]^2 + 4\hat{x} \cdot \hat{x}_j} - \frac{1 - \mathcal{L}(\hat{x}, \alpha_j)}{1 + \mathcal{L}(\hat{x}, \alpha_j)} (1 - \hat{x} \cdot \hat{x}_j) \right).$$

With the help of Theorem 4.1, $\lambda(\mathcal{G}(-\hat{x}, \hat{x}))$ is approximated by

$$\tilde{\lambda}(\hat{x}) := \frac{1}{2} \left(\lambda_{\alpha_1, \hat{x}}^{(\mathfrak{i})} + \lambda_{\alpha_2, \hat{x}}^{(\mathfrak{j})} \right), \quad (4.23)$$

where,

$$(\mathfrak{i}, \mathfrak{j}) = \arg \min_{(s, t) \in \{1, 2\} \times \{1, 2\}} \frac{|\lambda_{\alpha_1, \hat{x}}^{(s)} - \lambda_{\alpha_2, \hat{x}}^{(t)}|}{\sqrt{(\lambda_{\alpha_1, \hat{x}}^{(s)})^2 + (\lambda_{\alpha_2, \hat{x}}^{(t)})^2}}.$$

Note that

$$\left| \frac{d\lambda_{\alpha_j, \hat{x}}^{(1)}}{d\mathcal{L}} \right| = \left| \frac{(1 - \hat{x} \cdot \hat{x}_j) \frac{1+\mathcal{L}}{1-\mathcal{L}}}{\sqrt{[\frac{1+\mathcal{L}}{1-\mathcal{L}}(1 - \hat{x} \cdot \hat{x}_j)]^2 + 4\hat{x} \cdot \hat{x}_j}} - 1 \right| \frac{(1 - \hat{x} \cdot \hat{x}_j)}{(1 - \mathcal{L})^2} \leq \frac{2(1 - \hat{x} \cdot \hat{x}_j)}{(1 - \mathcal{L})^2}, \quad (4.24)$$

which implies that under the perturbation of noise, equation (4.22) remains stable when \mathcal{L} is far from 1, whereas the equation becomes ill-posed when $\mathcal{L} \approx 1$ ($\mathcal{L} = 1$ is equivalent to the case in which $\mathcal{B}u = u$ or $\mathcal{B}u = \partial u / \partial \nu$). This phenomenon also indicates that we need to select a larger α_j to keep \mathcal{L} away from 1 (note also that too large α_j will strengthen the residual term in (3.8), thereby making the algorithm less effective) and our criteria for determining the boundary conditions is reasonable.

4.1.2 Determine the boundary condition with given ∂D

Given ∂D , following Theorem 3.5, one may compute the impedance coefficient $\lambda(\mathcal{G}(-\hat{x}, \hat{x}))$ for $-\hat{x} \in \Theta_l$ via data on the direction set \mathcal{A}_1 . Specifically, for large k_- and k^+ , the impedance coefficient can be approximately calculated by

$$\lambda(\mathcal{G}(-\hat{x}, \hat{x})) \approx \frac{\mathcal{H} + 1}{\mathcal{H} - 1}, \quad (4.25)$$

where

$$\mathcal{H}(\hat{x}) := \frac{\sqrt{2\kappa(y^+)}}{M + 1} \sum_{m=0}^M u^{\infty, \delta}(\hat{x}, -\hat{x}, k_m) e^{-2ik_m y^+ \cdot \hat{x}}$$

with $y^+ = \mathcal{G}(-\hat{x}, \hat{x})$.

4.2 Direct sampling methods for the boundary

We introduce two direct sampling methods for shape reconstructions. Precisely, two indicators with and without boundary conditions, respectively, are proposed.

4.2.1 Shape reconstruction based on the computed boundary condition

Before introducing our direct sampling method, we may recall the Kirschhoff's approximation. For any convex obstacle D , let

$$\partial D_-(\theta) := \{x \in \partial D \mid \nu(x) \cdot \theta < 0\} \quad \text{and} \quad \partial D_+(\theta) := \{x \in \partial D \mid \nu(x) \cdot \theta \geq 0\} \quad (4.26)$$

be the illuminated region and shadow region, respectively, with respect to the incident direction θ . For a large wave number k , i.e., for a small wavelength, an obstacle D is locally almost a hyperplane with normal $\nu(x)$ at each point $x \in \partial D$. Consequently, the scattered field can be locally viewed as a reflected plane wave. For the near field, this implies that [12, 32]

$$u = 0 \text{ on } \partial D, \quad \frac{\partial u}{\partial \nu} \approx \begin{cases} 2 \frac{\partial u^{in}}{\partial \nu} & \text{on } \partial D_-(\theta); \\ 0 & \text{on } \partial D_+(\theta) \end{cases} \quad (4.27)$$

if D is sound soft, and

$$u \approx \begin{cases} 2u^{in} & \text{on } \partial D_-(\theta); \\ 0 & \text{on } \partial D_+(\theta). \end{cases} \quad \frac{\partial u}{\partial \nu} = 0 \text{ on } \partial D \quad (4.28)$$

if D is sound hard.

For the impedance case, under the same methodology, we assume that

$$u^s(y) \approx T(\theta, y) e^{ik\tilde{\theta}(y) \cdot x}, \quad y \in \partial D_-,$$

where $\tilde{\theta}(y) \in \mathbb{S}^{n-1}$ such that $\nu(y) = \mathcal{G}(\theta, \tilde{\theta})$. In addition, ignoring the derivative of T and $\tilde{\theta}$, we approximate boundary condition as follows

$$ik\lambda(y)(e^{ikx \cdot \theta} + T e^{ik\tilde{\theta} \cdot x}) + ik(\nu(y) \cdot \theta e^{ikx \cdot \theta} + T \nu(y) \cdot \tilde{\theta} e^{ikx \cdot \tilde{\theta}}) = 0, \quad \forall y \in \partial D_-.$$

Note that $\nu(y) \cdot \theta = -\nu(y) \cdot \tilde{\theta}(y)$, thus the scattered field has the following approximation

$$u \approx \begin{cases} u^{in} - \frac{\lambda + \nu \cdot \theta}{\lambda - \nu \cdot \theta} u^{in} & \text{on } \partial D_-(\theta); \\ 0 & \text{on } \partial D_+(\theta), \end{cases} \quad \text{and} \quad \frac{\partial u}{\partial \nu} \approx \begin{cases} \frac{\partial u^{in}}{\partial \nu} + \frac{\lambda + \nu \cdot \theta}{\lambda - \nu \cdot \theta} \frac{\partial u^{in}}{\partial \nu} & \text{on } \partial D_-(\theta); \\ 0 & \text{on } \partial D_+(\theta). \end{cases} \quad (4.29)$$

Inspired by the famous Bojarski identity [3], we deduce that

$$\begin{aligned} u^\infty(\hat{x}, -\hat{x}, k) &= \frac{C_n k^{(n-3)/2}}{2} \int_{\partial D} \left(\frac{\partial u}{\partial \nu} e^{-ik\hat{x} \cdot y} - u \frac{\partial e^{-ik\hat{x} \cdot y}}{\partial \nu} \right) ds(y) \\ &= \frac{C_n k^{(n-3)/2}}{2} \int_{\partial D} (-ik\lambda(y) + ik\hat{x} \cdot \nu(y)) u e^{-ik\hat{x} \cdot y} ds(y) \\ &\approx \frac{C_n k^{(n-3)/2}}{2} \int_{\partial D_-} (-ik\lambda(y) + ik\hat{x} \cdot \nu(y)) \left(1 - \frac{\lambda(y) - \nu(y) \cdot \hat{x}}{\lambda(y) + \nu(y) \cdot \hat{x}} \right) u^{in} e^{-ik\hat{x} \cdot y} ds(y) \\ &= \frac{C_n k^{(n-3)/2}}{2} \int_{\partial D_-} \frac{\lambda(y) - \nu(y) \cdot \hat{x}}{\lambda(y) + \nu(y) \cdot \hat{x}} (-2ik\hat{x} \cdot \nu(y)) e^{-2ik\hat{x} \cdot y} ds(y) \\ &\approx \frac{C_n k^{(n-3)/2}}{2} \gamma(\hat{x}) \int_{\partial D_-} \frac{e^{-2ik\hat{x} \cdot y}}{\partial \nu} ds(y), \quad \hat{x} \in S^{n-1}. \end{aligned}$$

Here, $C_2 = -e^{i\pi/4}/\sqrt{2\pi}$, $C_3 = -1/2\pi$ and $\gamma(\hat{x}) = \frac{\lambda(\mathcal{G}(-\hat{x}, \hat{x})) - 1}{\lambda(\mathcal{G}(-\hat{x}, \hat{x})) + 1}$. The final high frequency approximation is derived by the stationary phase method (Theorem 7.7.5 in [19]). Consequently, by

Green's theorem, we have

$$\begin{aligned}
& \gamma(\hat{x})^{-1}u^\infty(\hat{x}, -\hat{x}, k) + i^{3-n}\gamma(-\hat{x})^{-1}\overline{u^\infty(-\hat{x}, \hat{x}, k)} \\
& \approx \frac{C_n k^{(n-3)/2}}{2} \int_{\partial D} \frac{\partial e^{-2ik\hat{x}\cdot y}}{\partial \nu} ds(y) \\
& = \frac{C_n k^{(n-3)/2}}{2} \int_D \Delta e^{-2ik\hat{x}\cdot y} dy \\
& = -2C_n k^{(n+1)/2} \int_D e^{-2ik\hat{x}\cdot y} dy.
\end{aligned}$$

We rewrite it as

$$\int_{\mathbb{R}^n} \chi_D e^{-2ik\hat{x}\cdot y} dy \approx -\frac{\gamma(\hat{x})^{-1}u^\infty(\hat{x}, -\hat{x}, k) + i^{3-n}\gamma(-\hat{x})^{-1}\overline{u^\infty(-\hat{x}, \hat{x}, k)}}{2C_n k^{(n+1)/2}} =: V(\hat{x}, k). \quad (4.30)$$

Here, χ_D is the characteristic function of the domain D . $V(\hat{x}, k)$ can be viewed as the far field pattern of source χ_D in the direction \hat{x} and wave number $2k$.

Motivated by the indicators in [38] for the inverse source problem, we define the following indicator using the backscattering data:

$$I(z) := \frac{1}{l} \sum_{-\hat{x} \in \Theta_l} I_{\hat{x}}(z), \quad (4.31)$$

where

$$\begin{aligned}
I_{\hat{x}}(z) &:= \int_{k_-}^{k^+} k^{n-1} V(\hat{x}, k) e^{2ik\hat{x}\cdot z} dk \\
&= - \int_{k_-}^{k^+} \frac{\gamma(\hat{x})^{-1}u^\infty(\hat{x}, -\hat{x}, k) e^{2ik\hat{x}\cdot z} + i^{3-n}\gamma(-\hat{x})^{-1}\overline{u^\infty(-\hat{x}, \hat{x}, k)} e^{-2ik\hat{x}\cdot z}}{2C_n k^{(3-n)/2}} dk.
\end{aligned}$$

Letting l tend to infinity, we find that

$$\begin{aligned}
I(z) &\approx \frac{1}{2^{n-1}\pi} \int_{\mathbb{S}^{n-1}} I_{\hat{x}}(z) ds_{\hat{x}} \\
&\approx \frac{1}{2^{n-1}\pi} \int_{k_- < |\xi| < k^+} \int_{\mathbb{R}^n} \chi_D e^{-2i\xi\cdot y} dy e^{2i\xi\cdot z} d\xi \\
&= \frac{1}{2} \int_{k_- < |\xi| < k^+} \mathcal{F}[\chi_D](2\xi) e^{2i\xi\cdot z} d\xi.
\end{aligned}$$

This implies that $I(z)$ is again expected to capture the boundary ∂D when k_- is large because ∂D carries the high-frequency Fourier pattern of χ_D .

Numerically, we use the computed λ in (4.23), define

$$\tilde{\gamma}(\hat{x}) = \begin{cases} \frac{\tilde{\lambda}(\hat{x}) - 1}{\tilde{\lambda}(\hat{x}) + 1}, & \text{if (4.21) is established,} \\ 1, & \text{if (4.21) is not established,} \end{cases} \quad (4.32)$$

and plot the following indicator function on the domain of interest,

$$\mathcal{I}(z) = \frac{1}{l} \sum_{-\hat{x} \in \Theta_l} \mathcal{I}_{\hat{x}}(z), \quad (4.33)$$

where

$$\mathcal{I}_{\hat{x}}(z) := - \sum_{m=0}^M \frac{\tilde{\gamma}(\hat{x})^{-1} u^{\infty, \delta}(\hat{x}, -\hat{x}, k_m) e^{2ik_m \hat{x} \cdot z} + i \tilde{\gamma}(-\hat{x})^{-1} \overline{u^{\infty, \delta}(-\hat{x}, \hat{x}, k_m)} e^{-2ik_m \hat{x} \cdot z}}{2C_n k_m^{1/2}} \delta k.$$

Comparing (4.31) and (4.33), we drive that

$$\mathcal{I}(z) \approx \begin{cases} I(z), & \text{for Dirichlet condition,} \\ -I(z), & \text{for Neumann condition,} \\ I(z), & \text{for Impedance condition,} \end{cases}$$

which means that the indicator function $\mathcal{I}(z)$ is expected to catch the boundary ∂D . Moreover, $\mathcal{I}(z)$ can also be used to distinguish whether the boundary condition is the Dirichlet condition or the Neumann condition. We regard the boundary condition as

$$\mathcal{B}u = \begin{cases} u, & \text{if } \mathcal{I}|_{\partial D^+} < 0 < \mathcal{I}|_{\partial D^-}, \\ \frac{\partial u}{\partial \nu}, & \text{if } \mathcal{I}|_{\partial D^+} > 0 > \mathcal{I}|_{\partial D^-}. \end{cases} \quad (4.34)$$

Here, ∂D^\pm represent the outer and inner neighborhoods of ∂D . The explanation for criterion (4.34) can be obtained from the Gibbs phenomenon. Gibbs phenomenon is a classic phenomenon in signal processing and Fourier analysis, mainly manifested as fixed amplitude overshoot peak and oscillation near discontinuous points when approximating discontinuous periodic signals with finite M term Fourier series, details are shown in Figure 2. Note that I can be approximated by the difference between the $[k^+]$ -term Fourier series of χ_D and the $[k_-]$ -term Fourier series of χ_D .

4.2.2 Shape reconstruction without the boundary condition

On the other hand, owing to Theorem 3.1, we define the second indicator:

$$T(z) := \frac{1}{l} \sum_{-\hat{x} \in \Theta_l} \frac{|T_{\hat{x}}(z)|}{\sup_{y \in \mathbb{G}} |T_{\hat{x}}(y)|} \quad (4.35)$$

with

$$T_{\hat{x}}(z) := \int_{k_-}^{k^+} u^{\infty}(\hat{x}, -\hat{x}, k) e^{-2ik \hat{x} \cdot z} k^{(n-3)/2} dk, \quad z \in \mathbb{G}.$$

The behavior of $T_{\hat{x}}(z)$ is illuminated in the following proposition.

Proposition 4.2. *For a fixed $(\hat{x}, -\hat{x}) \in \mathcal{A}_2$, denote $y^+ = \mathcal{G}(-\hat{x}, \hat{x})$, we have*

$$T_{\hat{x}}(z) = \kappa^{-1/2}(y^+) R^\lambda(\hat{x}, -\hat{x}) \left((k^+)^{\frac{n-1}{2}} - (k_-)^{\frac{n-1}{2}} \right) + O\left(\ln \frac{k^+}{k_-}\right), \quad \text{if } (z - y^+) \cdot \hat{x} = 0$$

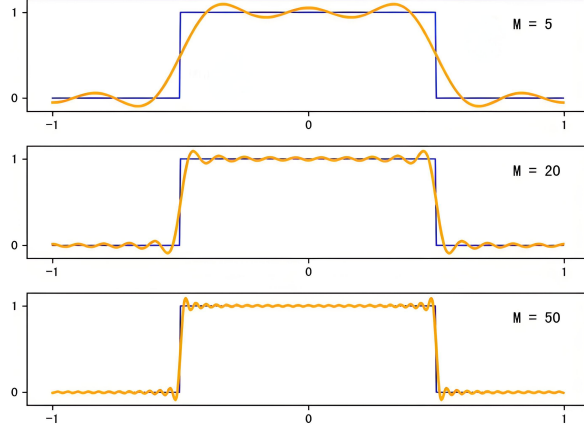


Figure 2: As M increases, the peak of finite M -term Fourier series gradually approaches discontinuous points.

Moreover, we have

$$T_{\hat{x}}(z) = O\left(\frac{k_-^{-\frac{3-n}{2}}}{|(z - y^+) \cdot \hat{x}|}\right) + O\left(\ln \frac{k^+}{k_-}\right)$$

for any z such that $(z - y^+) \cdot \hat{x} \neq 0$.

Proof. Inserting Theorem 3.1 into $T_{\hat{x}}$ in (4.35), we derive

$$\left| T_{\hat{x}}(z) - \int_{k_-}^{k^+} k^{\frac{n-3}{2}} \kappa^{-1/2}(y^+) R^\lambda(\hat{x}, -\hat{x}) e^{2ik(y^+-z) \cdot \hat{x}} dk \right| = O\left(\ln \frac{k^+}{k_-}\right).$$

The results follow by straightforward calculations if $(z - y^\pm) \cdot \hat{x} = 0$.

When $(z - y^+) \cdot \hat{x} \neq 0$, note that

$$\begin{aligned} \int_{k_-}^{k^+} e^{2ik(y^+-z) \cdot \hat{x}} dk &= \frac{1}{2i(y^+-z) \cdot \hat{x}} e^{2ik(y^+-z) \cdot \hat{x}} \Big|_{k_-}^{k^+} \\ &= O\left(\frac{1}{|(z - y^+) \cdot \hat{x}|}\right) \end{aligned}$$

for dimension $n = 3$ and that

$$\begin{aligned} \int_{k_-}^{k^+} k^{-\frac{1}{2}} e^{2ik(y^+-z) \cdot \hat{x}} dk &= \frac{k^{-\frac{1}{2}} e^{2ik(y^+-z) \cdot \hat{x}}}{2i(y^+-z) \cdot \hat{x}} \Big|_{k_-}^{k^+} + \frac{1}{2} \int_{k_-}^{k^+} \frac{e^{2ik(y^+-z) \cdot \hat{x}}}{2i(y^+-z) \cdot \hat{x}} k^{-\frac{3}{2}} dk \\ &= O\left(\frac{k_-^{-\frac{1}{2}}}{|(z - y^+) \cdot \hat{x}|}\right) + O\left(\int_{k_-}^{k^+} \frac{k^{-\frac{3}{2}}}{(y^+-z) \cdot \hat{x}} dk\right) \\ &= O\left(\frac{k_-^{-\frac{1}{2}}}{|(z - y^+) \cdot \hat{x}|}\right) \end{aligned}$$

for dimension $n = 2$. The proof is complete. \square

In conclusion, the indicator $T_{\hat{x}}(z)$ has a large value near the line $\{z \in \mathbb{R}^2 | (z - y^+) \cdot \hat{x} = 0\}$, which passes through $y^+ \in \partial D$, and decays when z is away from this line. We divide $T_{\hat{x}}(z)$ by $\sup_{y \in \mathbb{G}} |T_{\hat{x}}(y)|$ to counteract the effect of $\kappa^{-1/2}(y^+)R^\lambda(\hat{x}, -\hat{x})$. The boundary ∂D is consequently shown from the superposition of these lines, i.e., $T(z)$.

Numerically, we plot the following indicator function:

$$\mathcal{T}(z) = \frac{1}{l} \sum_{-\hat{x} \in \Theta_l} \frac{|\mathcal{T}_{\hat{x}}(z)|}{\sup_{y \in \mathbb{G}} |\mathcal{T}_{\hat{x}}(y)|}, \quad (4.36)$$

where

$$\mathcal{T}_{\hat{x}}(z) := \sum_{m=0}^M u^{\infty, \delta}(\hat{x}, -\hat{x}, k_m) e^{2ik_m \hat{x} \cdot z} k_m^{-1/2}, \quad z \in \mathbb{G}.$$

Obviously, $\mathcal{T}(z) \approx T(z)$. Therefore, $\mathcal{T}(z)$ is also expected to catch the boundary ∂D . Notably, the indicator $\mathcal{T}(z)$ requires less data than the indicator $\mathcal{I}(z)$, but the cost is that the boundary conditions cannot be determined.

4.3 Summary of reconstruction algorithm

Based on the methods proposed in the previous two subsections, we formulate Algorithm 1 for identifying an obstacle using the noisy multi-frequency backscattering far field patterns.

Algorithm 1: Reconstruct the boundary ∂D and identify boundary condition

Input: Far field data set $\left\{ u^{\infty, \delta}(\hat{x}, \theta, k) \middle| (\hat{x}, \theta) \in \mathcal{A}_2, k \in (k_-, k^+) \right\}$ with $Q_1 = -I$, $Q_2 = Q_{\alpha_1}$ and $Q_3 = Q_{\alpha_2}$ such that $\Theta_l = R_{\alpha_1} \Theta_l = R_{\alpha_2} \Theta_l$. Here, R_{α_1} , R_{α_2} , Q_{α_1} and Q_{α_2} are defined in (4.20) with $\alpha_1 = 8$ and $\alpha_2 = 10$.

Output: The boundary ∂D . The type of boundary condition. Furthermore, for impedance type scatterer D , output $\lambda(\mathcal{G}(-\hat{x}, \hat{x}))$, $\hat{x} \in \Theta_L$.

- 1 Compute $\mathcal{L}(\hat{x}, \alpha_j)$ in (4.19) for $-\hat{x} \in \Theta_l, j = 1, 2$.
 - 2 Follow (4.21), (4.22) and (4.23) to obtain $\tilde{\gamma}(\hat{x})$ in (4.32) for $-\hat{x} \in \Theta_l$. For impedance type scatterer, output $\lambda(\mathcal{G}(-\hat{x}, \hat{x}))$.
 - 3 Plot the indicator function $\mathcal{I}(z)$ to reconstruct ∂D .
 - 4 Use (4.34) to distinguish whether the boundary condition is the Dirichlet condition or the Neumann condition.
-

Remarks:

- One may use the indicator \mathcal{T} given by (4.36) directly to reconstruct the boundary ∂D . Different to \mathcal{I} given by (4.33), the behavior of the indicator \mathcal{T} is independent of the physical property of the obstacles.
- Given that ∂D is known or reconstructed in a high resolution (e.g., by the direct sampling method with the indicator \mathcal{T}), we can now compute the impedance coefficient λ by the formular (4.25). Note that the formular (4.25) is much more robust to measurement noises but highly rely on the resolution of ∂D since we have used the Gauss curvature.

5 Numerical examples and discussions

In this section, a variety of numerical examples are presented in two dimensions to illustrate the applicability and the effectiveness of our sampling methods. We consider the following two benchmark examples:

$$\text{Egg: } x(t) = \left(1.5 \cos t, \frac{\sin t}{1 + 0.2 \cos t} \right)^T, \quad -\pi \leq t \leq \pi, \quad (5.1)$$

$$\text{Kite: } x(t) = (\cos t + 0.65 \cos 2t - 0.65, 1.5 \sin t)^T, \quad -\pi \leq t \leq \pi. \quad (5.2)$$

Note that the egg shaped domain is convex, while the kite shaped domain is concave. In our simulations, if not stated otherwise, we will always consider equally distributed wave numbers with $\delta k = 0.1$ and 64 equally distributed directions of the incident wave in \mathbb{S}^1 . The grids are equally distributed on the rectangle $[-3, 3]^2$ with a sampling distance of 0.01.

For each example, we consider the following different boundary conditions:

- Dirichlet condition,
- Neumann condition,
- $\lambda_1(t) = 1 + 0.1 \sin(t)$, $-\pi < t < \pi$,
- $\lambda_2(t) = 2 + 0.5 \sin(t) + 0.2 \sin(5t)$, $-\pi < t < \pi$.

5.1 Reconstructions for the Egg Example

Following Algorithm 1, we begin by distinguishing between the following two scenarios:

- The scatterer D is either sound-soft or sound-hard.
- The scatterer D is of impedance type.

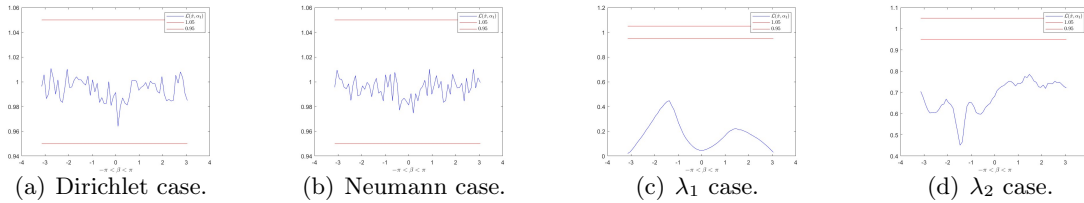
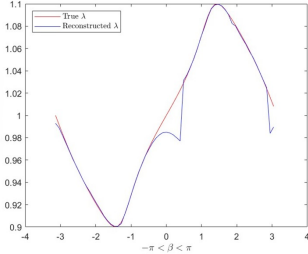
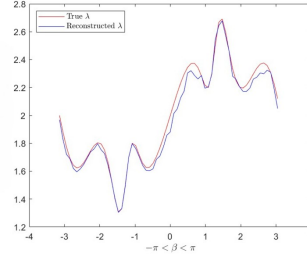


Figure 3: The values of $\mathcal{L}(\hat{x}, \alpha_1)$ for four different boundary conditions with frequency band $[20, 50]$.

Taking $\hat{x} = (\cos \beta, \sin \beta)^T$, $-\pi < \beta < \pi$. Based on the criteria (4.21), Figure 3 obviously show that the values of $\mathcal{L}(\hat{x}, \alpha_1)$ indeed lie in the interval $(0.95, 1.05)$ for the Dirichlet and the Neumann cases. Furthermore, Figure 4 shows the reconstruction of $\lambda(\mathcal{G}(-\hat{x}, \hat{x})) = \lambda(\beta)$ using (4.23). The reconstruction of λ is well-defined for values $\lambda \approx 1$, with the exception of the specific case when $\lambda = 1$. This is reasonable because $\mathcal{L} \rightarrow \infty$ as $\lambda \rightarrow 1$ in (4.22), and according to (4.24), it further makes the equation (4.22) so stable. However, \mathcal{L} is always calculated as a finite value, which is naturally not good for reconstruction in the case of $\lambda = 1$. Figure 5 shows the

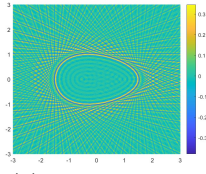


(a) Comparison for λ_1 .

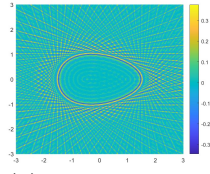


(b) Comparison for λ_2 .

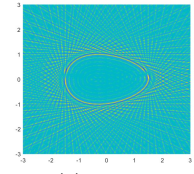
Figure 4: True and reconstructed λ_1 and λ_2 using (4.23) with frequency band $[20, 50]$.



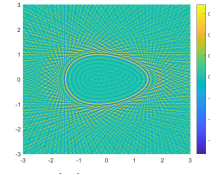
(a) Dirichlet case.



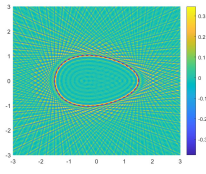
(b) Neumann case.



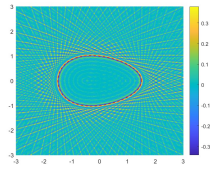
(c) λ_1 case.



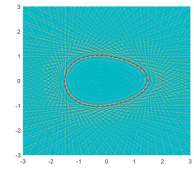
(d) λ_2 case.



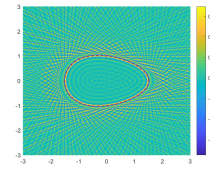
(e) Dirichlet case.



(f) Neumann case.



(g) λ_1 case.



(h) λ_2 case.

Figure 5: Reconstructions of ∂D with $\mathcal{I}(z)$ in different case using frequency band $[20, 50]$. Top: Plot of $\mathcal{I}(z)$. Bottom: Comparison with true ∂D (red dotted curve).

the effectiveness of the indicator function $\mathcal{I}(z)$. Owing to the high frequency data, these images seem somewhat not obvious. Using more low frequency data can improve this drawback for some examples. Although it is not compatible with the previous approximate theory, it is useful in practice. The details are shown in Figure 6. Note that in the λ_1 case, the indicator function $\mathcal{I}(z)$ obtained significantly larger values at two points than elsewhere, because $\lambda_1 \approx 1$ near these points and $\lambda = 1$ have indeed caused us trouble.

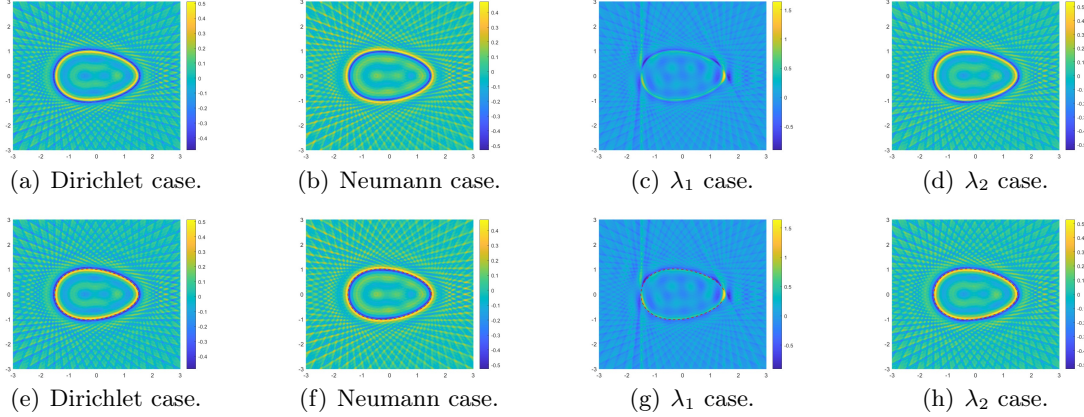


Figure 6: Reconstructions of ∂D with $\mathcal{I}(z)$ in different case using frequency band $[5, 30]$. Top: Plot of $\mathcal{I}(z)$. Bottom: Comparison with true ∂D (red dotted curve).

Meanwhile, Figure 5 and Figure 6 demonstrate the effectiveness of the judgment criteria (4.34). Furthermore, from the Gibbs phenomenon, ignoring the approximation error of the scattering field and choosing a smaller k_- and a larger k_+ can lead to more accurate judgment. Figure 7(a) and 7(b) confirm the validity of our inference. Figure 7(c) and 7(d) use the reconstructed λ from Figure 4, which implies that if the reconstructed impedance coefficient λ is not approximately 1, we can also use low-frequency data to obtain a good reconstruction of D or ∂D .

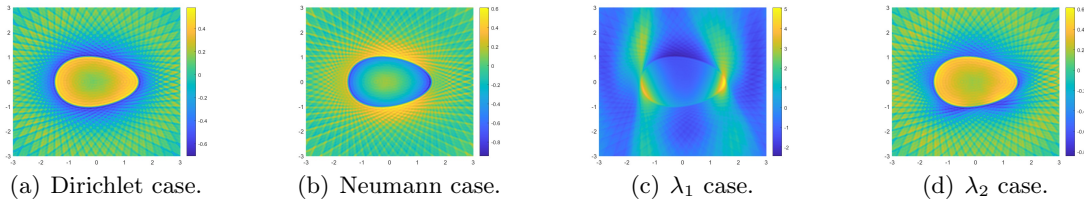


Figure 7: Reconstructions of ∂D with $\mathcal{I}(z)$ in different case using frequency band $[1, 30]$.

So far, we have completed the reconstruction for boundary conditions and boundary ∂D . Assuming that the boundary is exactly reconstructed, Figure 8 shows that with greater noise, the method (4.25) can effectively reconstruct the impedance coefficient λ .

We end this example with Figure 9. Figure 9 shows the reconstruction using the indicator function \mathcal{T} with sparse directional data. Similar to the analysis of Proposition 4.2, we capture these lines mentioned above. The reconstruction is improved with the increase of the observation direction number SD .

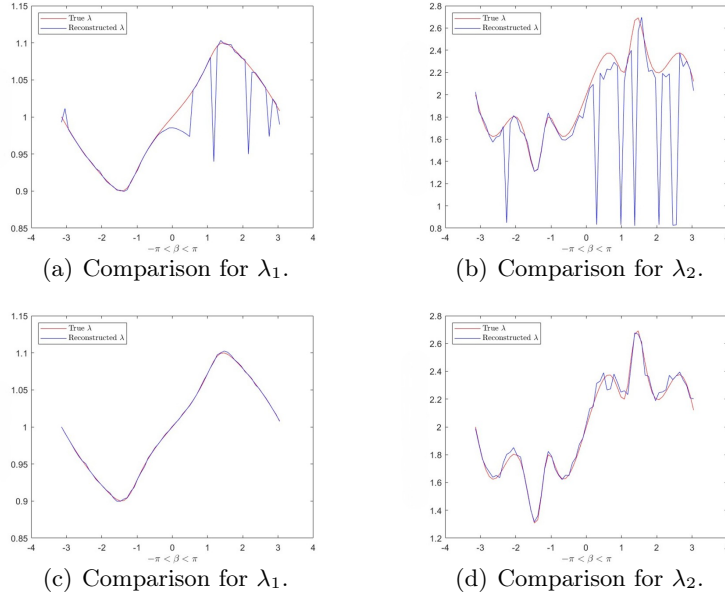


Figure 8: True and reconstructed λ_1 and λ_2 with $\delta = 0.3$ using frequency band $[20, 50]$. Top: Reconstructed λ by using (4.23). Bottom: Reconstructed λ by using (4.25).

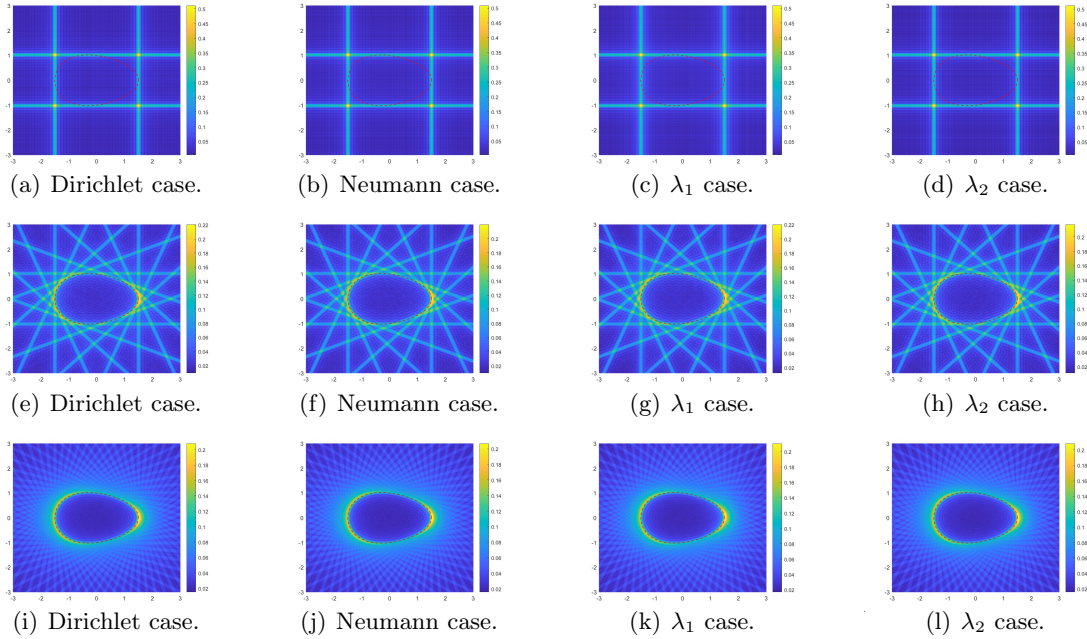


Figure 9: Reconstructions with $\mathcal{T}(z)$ in different cases using SD equally distributed directions data and frequency band $[20, 50]$, the true boundary ∂D is plotted by a red dotted curve. Top: $SD = 4$. Middle: $SD = 16$. Bottom: $SD = 64$.

5.2 Reconstructions for the Kite Example

For nonconvex obstacles, owing to the invalidity of the Theorem 3.8 for concave obstacles, we sometimes fail to determine whether their boundary conditions are Dirichlet or Neumann boundary conditions. Fortunately, changing the criteria (4.21) to the following criteria can effectively solve this problem,

$$\min_{\theta \in \Theta_l} |\mathcal{L}(\hat{x}, \alpha_j) - 1| < \frac{\delta}{2} = 0.05. \quad (5.3)$$

Figure 10 verifies the validity of the new criteria (5.3).

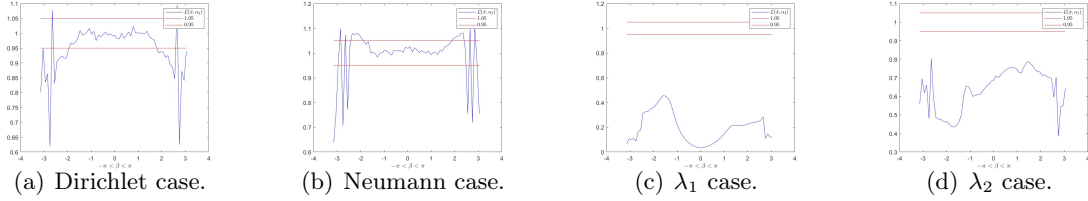


Figure 10: The values of $\mathcal{L}(\hat{x}, \alpha_1)$ for four different boundary conditions with frequency band $[20, 50]$.

Figure 11 shows the reconstruction of $\lambda(\mathcal{G}(-\hat{x}, \hat{x})) = \lambda(\beta)$, $-\pi < \beta < \pi$ using (4.23). Note that mapping $\mathcal{G}(\beta)$ is not injective with respect to β . Denote by $\Lambda_D \subset (-\pi, \pi)$ the component such that \mathcal{G} is injective. We observe that the impedance coefficient λ can be well reconstructed only in some subset of Λ_D .

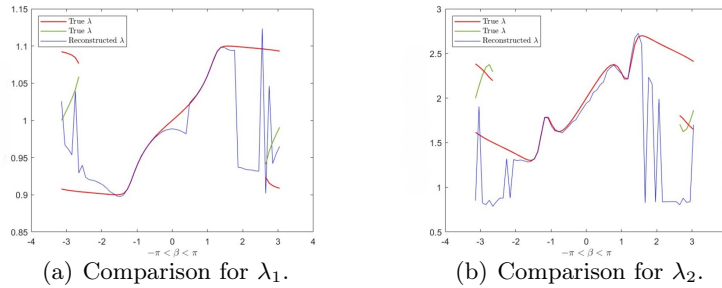


Figure 11: True and reconstructed λ_1 and λ_2 using (4.23) with frequency band $[20, 50]$.

Figures 12 and 13 illustrate that the indicator function $\mathcal{I}(z)$ and the criteria (4.34) can be used directly in concave situations. Surprisingly, $\mathcal{I}(z)$ performs very well in the Dirichlet and Neumann situations. Considering the poor reconstruction of λ on $(-\pi, \pi) \setminus \Lambda_D$, such reconstruction of ∂D for λ_1 and λ_2 case is acceptable. An interesting phenomenon worth discussing here is that for those λ near the concave structure, our algorithm always obtains the wrong solution in (4.23), note that for larger $\lambda > 1$, $\lambda_{\alpha_j, \hat{x}}^{(2)} \approx \sqrt{\hat{x} \cdot \hat{x}_j}$ is always the wrong solution. Thus, the wrong calculation $\gamma(\hat{x})^{-1}$ becomes large. It implies that the indicator function $\mathcal{I}(z)$ can properly reconstruct concave structures if the concave structure has a larger impedance coefficient λ , as shown in Figure 13(d) and 13(h).

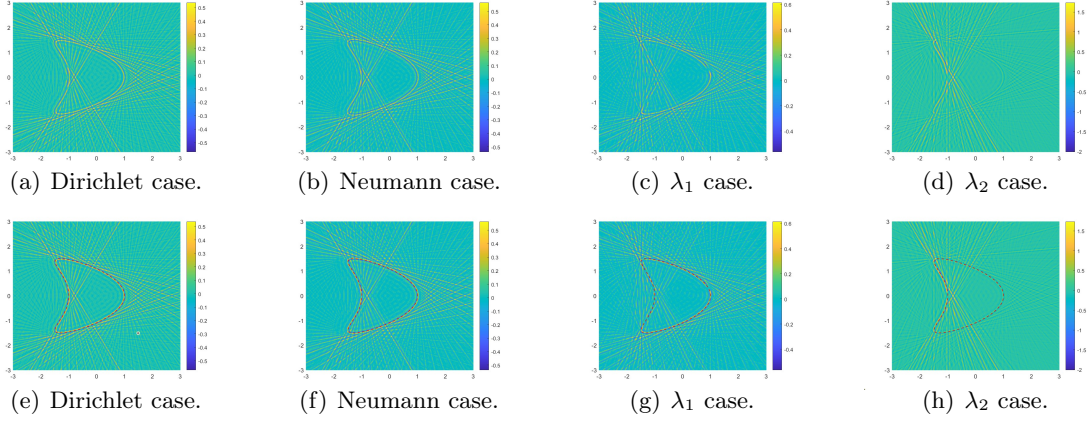


Figure 12: Reconstructions of ∂D with $\mathcal{I}(z)$ in different case using frequency band $[20, 50]$. Top: Plot of $\mathcal{I}(z)$. Bottom: Comparison with true ∂D (red dotted curve).

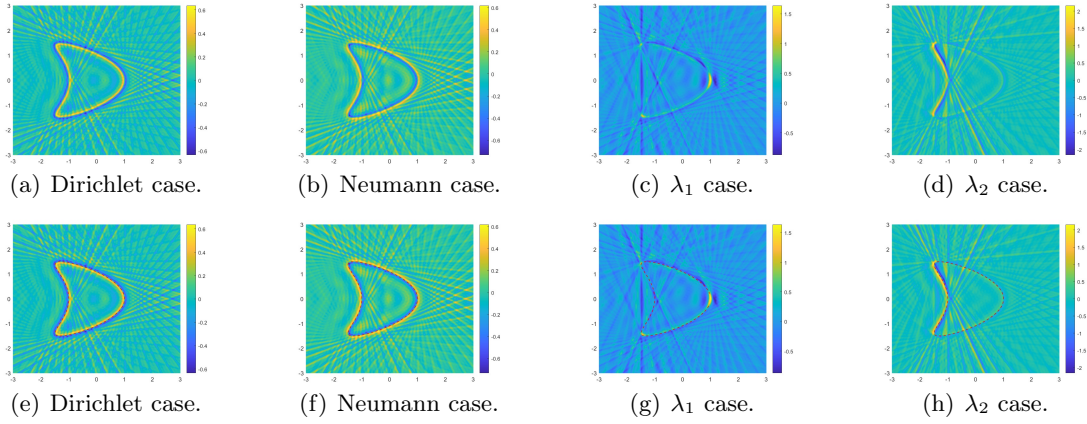


Figure 13: Reconstructions of ∂D with $\mathcal{I}(z)$ in different case using frequency band $[5, 30]$. Top: Plot of $\mathcal{I}(z)$. Bottom: Comparison with true ∂D (red dotted curve).

Figure 14 demonstrates that we can obtain a better reconstruction for λ via the method (4.25) with known ∂D . Note that λ received poor reconstruction near $\beta = -\pi$ because \mathcal{G} is not injective here.

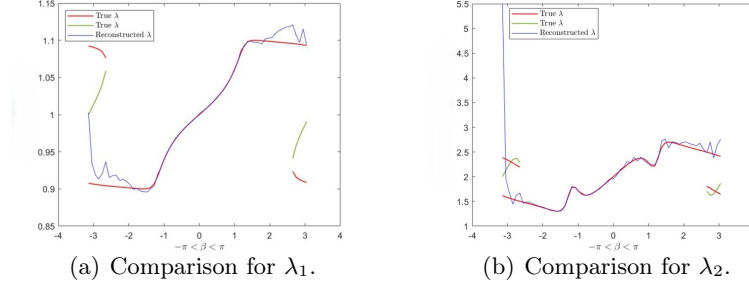


Figure 14: True λ_1 and λ_2 and reconstructed by (4.25) with $\delta = 0.3$ using frequency band $[20, 50]$.

Figure 15 shows that the indicator \mathcal{T} can reconstruct concave obstacles and has fairly good performance. The indicator \mathcal{T} is insensitive to changes in λ but is susceptible to the influence of high-curvature structures.

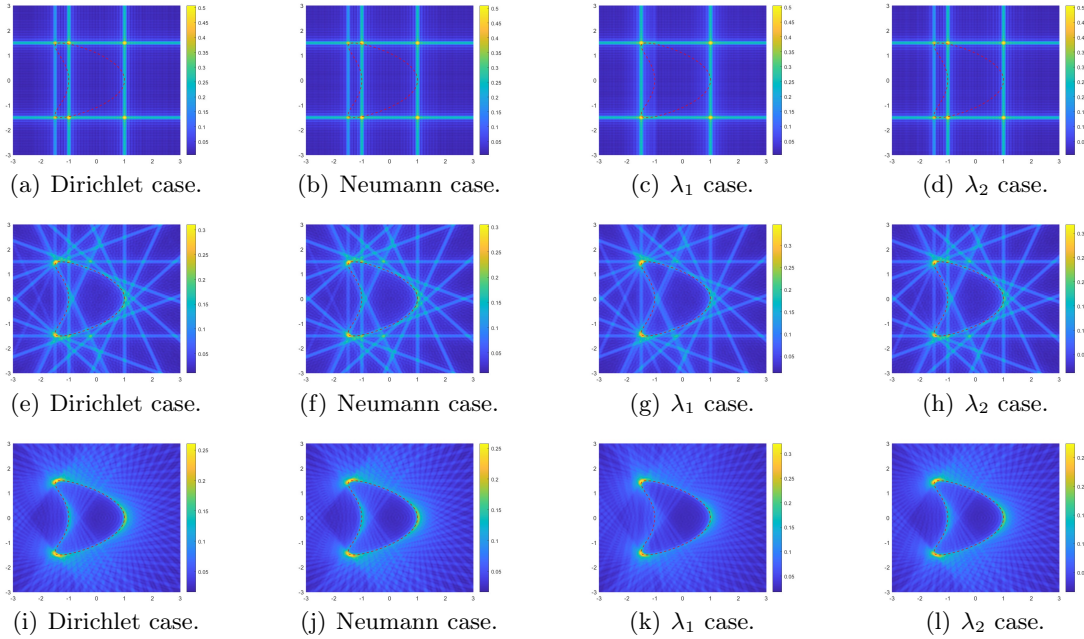


Figure 15: Reconstructions with $\mathcal{T}(z)$ in different cases using SD equally distributed directions data and frequency band $[20, 50]$, the true boundary ∂D is plotted by a red dotted curve. Top: $SD = 4$. Middle: $SD = 16$. Bottom: $SD = 64$.

Acknowledgement

The research of X. Liu is supported by the National Key R&D Program of China under grant 2024YFA1012303 and the NNSF of China under grant 12371430.

References

- [1] T. Arens, X. Ji and X. Liu, Inverse electromagnetic obstacle scattering problems with multi-frequency sparse backscattering far field data, *Inverse Probl.* **36**, (2020), 105007.
- [2] L. Beilina and M. V. Klibanov, A new approximate mathematical model for global convergence for acoefficient inverse problem with backscattering data, *J. Inverse Ill-Posed Probl.* **20**, (2012), 513–565.
- [3] N. Bojarski, A survey of the physical optics inverse scattering identity, *IEEE Trans. Antennas Propag.* **20** (1982), 980–989.
- [4] F. Cakoni and D. Colton, The determination of the surface impedance of a partially coated obstacle from far field data, *SIAM J. Appl. Math.* **64**, (2004), 709–723.
- [5] F. Cakoni, D. Colton and P. Monk, The determination of boundary coefficients from far field measurements, *J. Integr. Equations Appl.* **22(2)** (2010), 167–191.
- [6] S. N. Chandler-Wilde, I. G. Graham, S. Langdon and E.A. Spence, Numerical asymptotic boundary integral methods in high-frequency acoustic scattering, *Acta Numer.* **21** (2012), 89–305.
- [7] J. Chen, Z. Chen and G. Huang, Reverse time migration for extended obstacles: acoustic Waves, *Inverse Probl.* **29** (2013), 085005.
- [8] J. Cheng, J. Liu and G. Nakamura, Recovery of the shape of an obstacle and the boundary impedance from the far field pattern, *Kyoto J. Math.* **43**, (2003).
- [9] D. Colton, Stable methods for determining the surface impedance of an obstacle from low frequency far field data, *Appl. Anal.* **14**, (1982), 61–70.
- [10] D. Colton and A. Kirsch, The determination of the surface impedance of an obstacle from measurements of the far field pattern, *SIAM J. Appl. Math.* **41**, (1981), 8–15.
- [11] D. Colton and A. Kirsch, A simple method for solving inverse scattering problems in the resonance region, *Inverse Probl.* **12**, (1996), 383–393.
- [12] D. Colton and R. Kress, *Inverse Acoustic and Electromagnetic Scattering Theory* (Fourth Edition), Springer, Berlin, 2019.
- [13] D. Colton and P. Monk, Target identification of coated objects, *IEEE Trans. Antennas Propagat.* **54**, (2006), 1232–1242.
- [14] F. Dou, X. Liu, S. Meng and B. Zhang, Data completion algorithms and their applications in inverse acoustic scattering with limited-aperture backscattering data, *J. Comput. Phys.* **469**, (2022), 111550.
- [15] G. Eskin and J. Ralston, The inverse backscattering problem in three dimensions, *Commun. Math. Phys.* **124** (1989), 169–215.
- [16] G. Eskin and J. Ralston, Inverse backscattering problem in two dimensions, *Commun. Math. Phys.* **138** (1991), 456–486.

- [17] R. Griesmaier, N. Hyvönen and O. Seiskari, A note on analyticity properties of far field patterns, *Inverse Probl. Imag.* **7**, (2013), 491–498.
- [18] L. He, S. Kindermann and M. Sini, Reconstruction of shapes and impedance functions using few far field measurements, *J. Comput. Phys.* **228**, (2009), 717–730.
- [19] L. Hörmander, *The Analysis of Linear Partial Differential Operators I: Distribution Theory and Fourier Analysis* (2nd Edition), Springer, Berlin Heidelberg, 2003.
- [20] K. Ito, B. Jin, and J. Zou, A direct sampling method to an inverse medium scattering problem, *Inverse Probl.* **28** (2012), 025003.
- [21] O. Ivanyshyn and R. Kress, Inverse scattering for surface impedance from phase-less far field data, *J. Comput. Phys.* **230**, (2011), 3443–3452.
- [22] A. W. Kędzierawski, The determination of the surface impedance of an obstacle, *Proc. Edinburgh Math. Soc.* **36**, (1993), 1–15.
- [23] A. Kirsch, Optimal control of an exterior robin problem, *J. Math. Anal. Appl.* **82**, (1981), 144–151.
- [24] A. Kirsch, Characterization of the shape of a scattering obstacle using the spectral data of the far field operator, *Inverse Probl.* **14** (1998), 1489–1512.
- [25] A. Kirsch and N. Grinberg, *The Factorization Method for Inverse Problems*, Oxford University Press, 2008.
- [26] R. Kress, On the numerical solution of a hypersingular integral equation in scattering theory, *J. Comput. Appl. Math.* **61** (1995), 345–360 .
- [27] R. Kress and W. Rundell, Inverse obstacle scattering using reduced data, *SIAM J. Appl. Math.* **59** (1998), 442–454.
- [28] R. Kress and W. Rundell, Inverse scattering for shape and impedance, *Inverse Probl.* **17**, (2001), 1075–1085.
- [29] R. Kress and W. Rundell, Inverse scattering for shape and impedance revisited, *J. Integr. Equations Appl.* **30**, (2018), 293–331.
- [30] R. Lagergren, The back-scattering problem in three dimensions, *J Pseudo-Differ. Oper.* **2**, (2011), 1–64.
- [31] K.-M. Lee, Inverse scattering problem from an impedance obstacle via two-steps method, *J. Comput. Phys.* **274**, (2014), 182–190.
- [32] J. Li and H. Liu, Recovering a polyhedral obstacle by a few backscattering measurements, *J. Differ. Equations* **259** (2015), 2101–2120.
- [33] J. Li, H. Liu and Y. Wang, Recovering an electromagnetic obstacle by a few phaseless backscattering measurements, *Inverse Probl.* **33**, (2017), 035011.

- [34] J. Li, H. Liu and J. Zou, Locating multiple multiscale acoustic scatterers, *SIAM Multi. Model. Simul.* **12** (2014), 927-952.
- [35] J. Li and J. Zou, A direct sampling method for inverse scattering using far field data, *Inverse Probl. Imag.* **7** (2013), 757-775.
- [36] J. Liu, G. Nakamura and M. Sini, Reconstruction of the shape and surface impedance from acoustic scattering data for an arbitrary cylinder, *SIAM J. Appl. Math.* **67**, (2007), 1124-1146.
- [37] X. Liu, A novel sampling method for multiple multiscale targets from scattering amplitudes at a fixed frequency, *Inverse Probl.* **33** (2017), 085011.
- [38] X. Liu and Q. Shi, A quantitative sampling method for elastic and electromagnetic sources, arXiv:2503.06581, 2025.
- [39] X. Liu and J. Sun, Data recovery in inverse scattering: from limited-aperture to full-aperture, *J. Comput. Phys.* **386(1)** (2019), 350-364.
- [40] D. Ludwig, Uniform asymptotic expansion of the field scattered by a convex object at high frequencies, *Commun. Pure Appl. Math.* **20(1)** (1967), 187-203
- [41] A. Majda, High frequency asymptotics for the scattering matrix and the inverse problem of acoustical scattering, *Commun. Pure Appl. Math.* **29(3)** (1976), 261-291.
- [42] W. Mclean, *Strongly Elliptic Systems and Boundary Integral Equation*, Cambridge University Press, Cambridge, 2000.
- [43] C. Morawetz, Decay for solutions of the exterior problem for the wave equation, *Commun. Pure Appl. Math.* **28(2)** (1975), 229-264.
- [44] P. Ola, L. Päiväranta and V. Serov, Recovering singularities from backscattering in two dimensions, *Commun. Part. Diff. Equat.* **26**, (2001), 697-715.
- [45] R. Potthast, A study on orthogonality sampling, *Inverse Probl.* **26** (2010), 074075.
- [46] Rakesh and G. Uhlmann, Uniqueness for the inverse backscattering problem for angularly controlled potentials, *Inverse Probl.* **30**, (2014), 065005.
- [47] V. Serov, Inverse fixed angle scattering and backscattering problems in two dimensions, *Inverse Probl.* **24**, (2008), 065002.
- [48] P. Serranho, A hybrid method for inverse scattering for shape and impedance, *Inverse Probl.* **22**, (2006), 663-680.
- [49] J. Shin, Inverse obstacle backscattering problems with phaseless data, *Eur. J. Appl. Math.* **27**, (2016), 111-130.
- [50] E. Spence, Wavenumber-Explicit Bounds in Time-Harmonic Acoustic Scattering, *SIAM J. Math. Anal.* **46(4)**, (2014) 2987-3024.

- [51] P. Stefanov and G. Uhlmann, Inverse backscattering for the acoustic equation, *SIAM J. Math. Anal.* **28** (1997), 1191-1204.
- [52] M. Taylor, Grazing rays and reflection of singularities of solutions to wave equations, *Commun. Pure Appl. Math.* **29(1)**, (1976), 1-37.
- [53] G. Uhlmann, A time-dependent approach to the inverse backscattering problem, *Inverse Probl.* **17**, (2001), 703–716.
- [54] J.-N. Wang, Inverse backscattering problem for the acoustic equation in even dimensions, *J. Math. Anal. Appl.* **220**, (1998), 676–696.